Journal of
Synchrotron Radiation

ISSN 0909-0495

Received 23 March 2009
Accepted 18 May 2009

Multiple-element spectrometer for non-resonant inelastic X-ray spectroscopy of electronic excitations

Roberto Verbeni,[a] Tuomas Pylkkänen,[a,b] Simo Huotari,[a] Laura Simonelli,[a] György Vankó,[a,c] Keith Martel,[a] Christian Henriquet[a] and Giulio Monaco[a]

[a]European Synchrotron Radiation Facility, Boîte Postale 220, F-38043 Grenoble Cedex 9, France, [b]Division of Materials Physics, Department of Physics, FI-00014 University of Helsinki, Finland, and [c]KFKI Research Institute for Particle and Nuclear Physics, H-1525 Budapest, POB 49, Hungary

A multiple-analyser-crystal spectrometer for non-resonant inelastic X-ray scattering spectroscopy installed at beamline ID16 of the European Synchrotron Radiation Facility is presented. Nine analyser crystals with bending radii $R = 1$ m measure spectra for five different momentum transfer values simultaneously. Using a two-dimensional detector, the spectra given by all analysers can be treated individually. The spectrometer is based on a Rowland circle design with fixed Bragg angles of about 88°. The energy resolution can be chosen between 30–2000 meV with typical incident-photon energies of 6–13 keV. The spectrometer is optimized for studies of valence and core electron excitations resolving both energy and momentum transfer.

Keywords: inelastic X-ray scattering; X-ray spectroscopy; crystal analyser.

1. Introduction

Inelastic X-ray scattering (IXS) spectroscopy is a rapidly developing tool for studies of the electronic structure of matter (Schülke, 2007). Both instrumentation and theoretical understanding have improved greatly in the past few years. The experimental method can be divided into resonant and non-resonant IXS (RIXS and NRIXS, respectively). Each method has rather different instrumental requirements, and it is not easy to conceive a spectrometer which is optimized for all applications simultaneously. However, there are a few issues that are common to all modern IXS spectrometers. First of all, they are all based at synchrotron radiation facilities, as the high flux and energy tunability of synchrotron radiation are prerequisites for any modern IXS study. Secondly, as standard X-ray detectors in the 5–20 keV range feature typically only a resolution of a few hundred eV, with the exceptions of specialized superconducting tunnel junction detectors (Frank *et al.*, 1996; Mears *et al.*, 1996) or microbolometers (Alessandrello *et al.*, 1999), the high-resolution IXS instruments at the moment are based on crystal-analyser spectrometers. The very narrow bandpass of a high-quality single crystal, typically silicon or germanium, allows the spectrum of hard X-rays to be resolved with high accuracy.

The spectrometer presented here is specialized in NRIXS. The interest in NRIXS mostly resides in the fact that the double-differential cross section is readily understood in terms of the longitudinal dielectric function. Several *ab initio* methods exist for the corresponding calculations, and the results can be compared with several other techniques that also probe the dielectric function. The probability of scattering to a solid-angle element $[\Omega, \Omega + d\Omega]$ and an energy-transfer range $[\omega, \omega + d\omega]$ (with $\hbar = 1$) is (Schülke, 2007)

$$\frac{d^2\sigma}{d\Omega d\omega} = \left(\frac{d\sigma}{d\Omega}\right)_{Th} S(\mathbf{q}, \omega), \tag{1}$$

where $(d\sigma/d\Omega)_{Th}$ is the Thomson scattering cross section (specific for X-ray scattering from electrons), and $S(\mathbf{q}, \omega)$ is the dynamic structure factor, which is in turn related to the longitudinal dielectric function $\varepsilon_L(\mathbf{q}, \omega)$,

$$S(\mathbf{q}, \omega) = -\frac{q^2}{4\pi^2 e^2} \, \mathrm{Im}\left[\varepsilon_L(\mathbf{q}, \omega)\right]^{-1}. \tag{2}$$

A similar function is probed by electron-energy-loss spectroscopy (EELS) (García de Abajo, 2009). IXS is typically used when bulk sensitivity, the ability to penetrate through different sample environments, and large momentum transfers are looked for. In turn, the IXS cross section is very small, which often leads to lengthy measurements and to the choice of using lower resolution in energy and momentum transfer. The combination of these advantages and disadvantages defines a class of scientific problems where IXS can give very useful or even unique information (Schülke, 2007).

Several synchrotron radiation sources nowadays host instruments for NRIXS studies for electronic excitations (Cai *et al.*, 2004; Hill *et al.*, 2007; Fister *et al.*, 2006; Bergmann & Cramer, 1998; Hazemann *et al.*, 2009). Some of them feature multiple analyser crystals to increase the solid angle collected

by the detector unit. The purpose of this contribution is to describe the nine-element spectrometer set-up developed at the beamline ID16 of the European Synchrotron Radiation Facility (ESRF), in Grenoble, France. The article is arranged as follows. Some general considerations about the spectrometer design are reported in §2. The analysers and their mounting are described in §3. The detector and its operation are presented in §4, and the contributions to the momentum and energy resolutions are discussed in §5. Examples of typical applications and the performance of the instrument are shown in §6, and finally conclusions are drawn in §7.

2. Beamline set-up for non-resonant inelastic X-ray scattering

At ID16, the incident beam is generated by three consecutive undulators and premonochromatized by a liquid-nitrogen-cooled double-crystal Si(111) monochromator. The bandwidth from the premonochromator is 1.1 eV at 10 keV for a 25 µrad vertical divergence of the undulator radiation. Additional reduction of the incident-beam bandwidth can be achieved with a channel cut in a total four-crystal (+,−,−,+) configuration together with the premonochromator. Typical photon energies used in the experiments, the corresponding analyser crystals, possible channel-cut reflections, resulting bandwidths, and fluxes at the sample are reported in Table 1.

After the monochromator ensemble, the beam can be focused using a Rh-coated toroidal mirror, resulting in a typical focal spot size of about 50 µm × 130 µm (V × H). For radiation-sensitive samples, such as polymers, certain liquids *etc.*, the local power density may be too large and radiation damage or local heating may become a problem. In this case, and if the sample is large enough, the focusing option can be avoided and an unfocused beam (1 mm × 2 mm) can be used. The beamline layout is presented in Fig. 1.

Energy scans are performed in the so-called inverse geometry, where the incident-photon energy $E_1 = E_2 + \omega$ is scanned, observing scattered intensity at a fixed photon energy E_2. This makes the design of the spectrometer easier; most importantly the efficiency of the spectrometer (owing to, for example, analyser crystal reflectivity) is constant throughout the energy scan.

Important factors that guided the design of the instrument were (i) suitability for a variety of applications, (ii) modularity, (iii) efficiency and (iv) tunable resolution in energy and momentum transfers. A good compromise for both studies of valence and core-electron excitations was found to be met by a set-up where the analyser crystal arrangement is suitable for recording the signal at several different scattering angles simultaneously, but keeping a large number of analysers at either low or high momentum-transfer regions. Valence-electron excitations may be rapidly dispersing with **q**, necessitating an accurately tunable **q**. The core-excitation momentum-transfer dependence is smaller, and generally requires a measurement at only one to three distinctly separate momentum transfer settings in the range 1–10 Å^{-1} (Soininen *et al.*, 2006; Galambosi *et al.*, 2006). The chosen design is a configuration of 1 + 2 × 4 = 9 analysers in the horizontal scattering geometry with vertical Rowland circles. The analyser-crystal array is shown in Fig. 2. The active size of the analyser crystals can be reduced if necessary by slits which can also be seen in Fig. 2 (horizontal and vertical slits for the first analyser on the right, horizontal only for all others).

A drawing of the exterior of the spectrometer is presented in Fig. 3. The analysers are inside a vacuum chamber to minimize air absorption and background scattering. The spectrometer is mounted on a table, in which the sample goniometer is also integrated, and the table can be aligned to the beam using motorized movements. The main rotation

Table 1
Typically used analyser photon energies E_2 and the corresponding analyser crystal reflections used for experiments with the current design; certain corresponding available monochromatization schemes, resulting incident-beam bandwidths and fluxes at the sample position normalized to a nominal maximum ring current of 200 mA are also listed; the flux was measured using a 300 µm-thick Si pin diode (Owen *et al.*, 2009).

E_2 (keV)	Analyser reflection	Channel-cut	Incident-beam bandwidth (meV)	Intensity (photons s^{-1})
5.93	Si(333)	None	650	1.4×10^{13}
5.93	Si(333)	Si(333)	52	6.2×10^{11}
6.46	Si(440)	Si(220)	300	2.6×10^{12}
7.91	Si(444)	Si(444)	39	1.1×10^{12}
9.69	Si(660)	None	1200	7.0×10^{13}
9.69	Si(660)	Si(220)	400	1.5×10^{13}
9.69	Si(660)	Si(440)	200	3.5×10^{12}
9.69	Si(660)	Si(444)	140	1.5×10^{12}
9.89	Si(555)	Si(555)	15	3.2×10^{11}
12.9	Si(880)	None	2100	7.0×10^{13}
13.8	Si(777)	Si(777)	5.0	1.0×10^{11}
16.2	Si(10,10,0)	None	3200	6.0×10^{13}

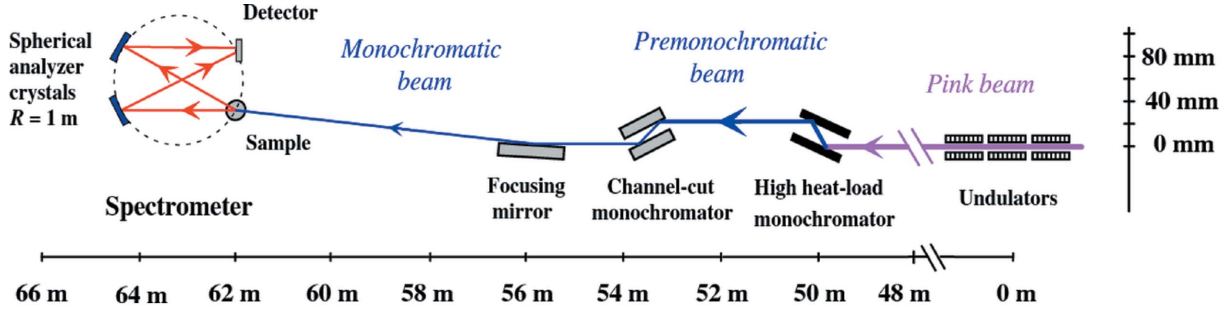

Figure 1
ID16 beamline layout relevant for the electronic excitation studies.

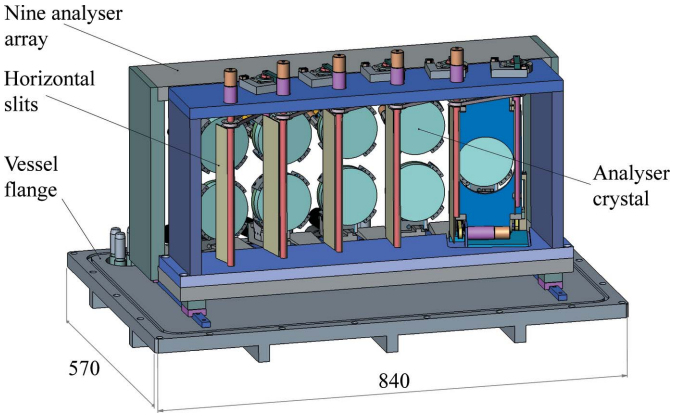

Figure 2
The analyser-crystal array with its slit assembly. The lone analyser on the right is the one that can reach the lowest momentum transfer. The dimensions are in millimetres.

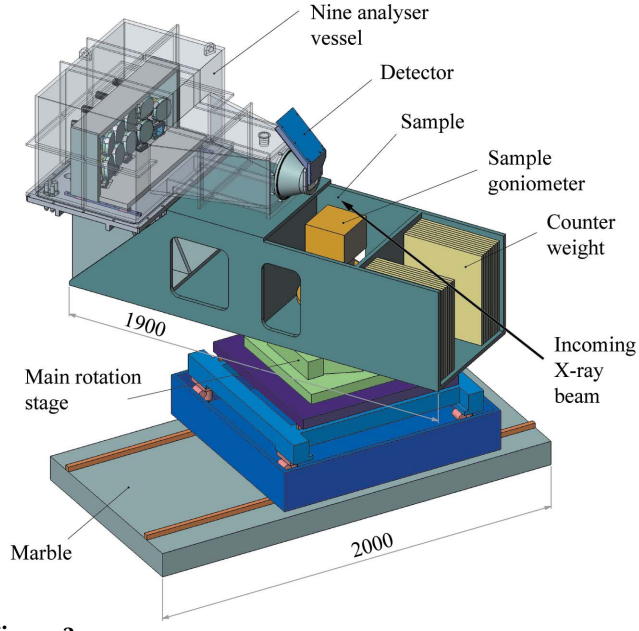

Figure 3
Schematic design of the spectrometer with its vacuum chamber rendered partly transparent and slit assembly not shown for clarity. The dimensions are in millimetres.

stage (shown in green) is used to select the momentum transfer setting.

The Rowland circles are vertical since the source size given by the toroidal mirror is smaller in the vertical than in the horizontal direction, minimizing the geometrical contribution of the source size to the energy resolution. On the other hand the scattering plane (synchrotron–sample–analyser) is chosen to be horizontal in order to decouple it from the Rowland-circle plane (sample–analyser–detector). This ensures that (i) any source-size broadening owing to a long footprint in cases of thick samples or grazing incidence on a sample surface has a negligible effect on the energy resolution, and (ii) the energy calibration is not sensitive to the position of the sample along the incident-photon beam. However, this geometry comes with a price to pay. Since the scattering plane is parallel to the plane of the synchrotron electron beam orbit, the Thomson scattering cross section reads $(\mathrm{d}\sigma/\mathrm{d}\Omega)_{\mathrm{Th}} = r_e^2(E_2/E_1)\cos^2 2\theta$, where r_e is the classical electron radius and 2θ is the scattering angle. This means that the region around $2\theta = 90^\circ$ is not accessible owing to a vanishing scattering cross section in that direction.

3. Analyser crystals

All analysers are of the spherical Johann type with curvature radii R = 990–1010 mm. A multiple choice of analyser crystals is available. Mostly used are diced Si(*nnn*) crystals for high-resolution studies (10–300 meV with n = 3–7), or bent Si(*nnn*)/Si(*nn*0) crystals for applications which do not require very high resolution but where a higher luminosity is welcome (n = 3–8 with resolutions 500–2000 meV). All analyser crystals are constructed starting from 100 mm-diameter Si wafers. The analyser fabrication methods and characterization schemes are reviewed by Verbeni *et al.* (2005). Typical analyser crystals are show in Fig. 4. A diced analyser crystal (Fig. 4*a*) consists of $\sim 10^4$ individual cubes that are glued onto a spherical surface. The wafer thickness $T \simeq 2$ mm is larger than the dice size $c \simeq 0.7$ mm, which makes each dice unstrained on the reflecting surface, its bandpass given by the dynamical diffraction theory (Prince–Darwin curve) (Masciovecchio *et al.*, 1996; Schwoerer-Böhning *et al.*, 1998).

The bent crystals for lower energy-resolution applications (Fig. 4*b*) are single wafers of thickness 500 µm attached to concave glass blanks with the anodic bonding technique (Verbeni *et al.*, 2005). Owing to the bending, such a large-area monolithic crystal typically exhibits more elastic deformation

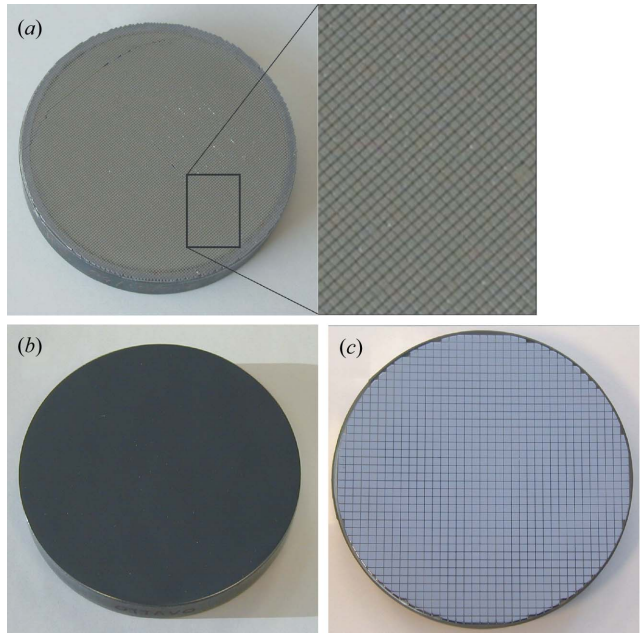

Figure 4
Typical analyser crystals used at ID16. (*a*) Diced crystal for high-resolution applications, thickness 2 mm and a cube size 0.7 mm (detail zoomed in); (*b*) bent crystal for low-resolution applications, anodic bonded to the glass substrate; (*c*) stress-relief-cut crystal for medium-resolution applications, thickness 250 µm, period 2.5 mm. All crystal wafers have a diameter of 100 mm.

than for a nominal perfect spherical bending. This deteriorates its properties in both energy resolution and focusing when compared with those expected theoretically (Taupin, 1964; Takagi, 1962; Takagi, 1969).

In order to improve the bent-analyser energy resolution, construction techniques with the aim of releasing the stress of a bent large-area wafer have been developed (Schwoerer-Böhning *et al.*, 1998; Shew *et al.*, 2002). In our case, we have used a 500 μm-thick Si wafer cut with a diamond saw into a raster of 2.5 mm × 2.5 mm, leaving a backwall of thickness 200 μm. The wafer is attached to a glass substrate with the anodic bonding technique from the cut side and the remaining backwall is removed by chemical etching, much like in the construction technique of the diced analysers (Verbeni *et al.*, 2005). As a result these stress-relief-cut crystals (Fig. 4*c*) consist of hundreds of bent crystallites with a surface area of a few mm^2 each. The basic difference between these and diced analysers is the ratio c/T. Here, it is larger than 1 with c = 2.5 mm and $T \simeq 250$ μm, making the individual dices bent. However, owing to their small size, unwanted deformations are reduced and bandwidths close to the theoretically expected ones can be reached, as will be discussed further in §5. The possibility to control the final resolution by fine tuning the ratio c/T is currently being studied.

A single analyser–goniometer unit is presented in Fig. 5. The goniometer is based on motorized micrometre screws, each with a range of 4 mm. The screw pushes the goniometer unit at 42 mm distance from the centre, giving a close to linear correspondence between the translation of the screw tip and the achieved change of the Bragg angle of the analyser, with a total tunable range of 5°. The pusher has a resolution of 100 nm, giving an angular resolution of the goniometer of about 2 μrad. All analyser goniometers are mounted on linear translations with positioning ranges of 30 mm in order to compensate for differences in the bending radii of the analysers.

In addition, the full analyser assembly is mounted on a linear translation stage with a positioning range of 100 mm.

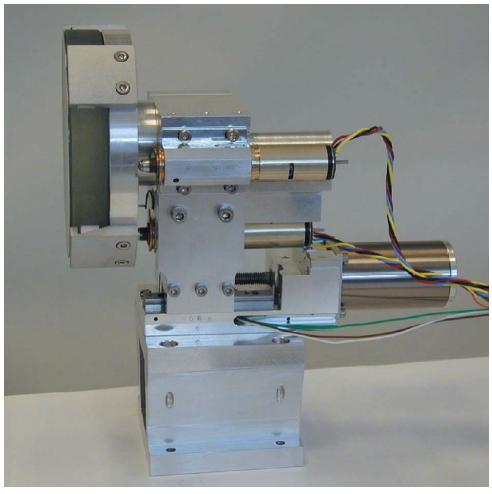

Figure 5
Single goniometer unit with a bent crystal mounted.

These adjustable positions make it possible to work either with both the detector and all analysers on the Rowland circles, or with the detector 50–150 mm inside the Rowland circles (corresponding to analyser displacements of 25–75 mm away from the sample) for applications that require a large sample environment. Changing all nine analysers is typically about a 1 h operation, so it can be rather conveniently carried out even during an experiment.

4. Detector unit

The detecting system is based on a Maxipix (multichip assembly for X-ray imaging based on a photon counting pixel array) detector, which exploits the Medipix2 (Llopart *et al.*, 2002) readout chip. It consists of 256 × 256 pixels each of 55 μm × 55 μm. The thickness of the active Si layer is 500 μm. As for every part of the spectrometer, the detector is also a modular unit that can be replaced by other types of detectors if necessary. The detector is not under vacuum, but rather immediately after a Kapton window which separates the analyser crystal vacuum chamber from the hutch atmosphere.

The nine foci of the analysers can be guided on different areas on the detector, and thus the spectra corresponding to each analyser can be saved and processed separately. This is true with both diced and bent crystals. The position-sensitive detector offers several advantages compared with an array of point detectors. For instance, it allows for the direct observation of the energy dispersion within a focal spot of a diced analyser crystal (Huotari *et al.*, 2005, 2006). Another important application of the position information is based on the point-to-point focusing capability of a bent analyser. While choosing the desired bandwidth in energy, it also produces a mirror image of the beam path within the sample, as shown schematically in Fig. 6(*a*). This takes place within the focusing capabilities of the analyser, in practice with a spatial resolution of the order of 100–300 μm. This can be extremely useful if the beam penetration within the sample is $\gtrsim 1$ mm, giving the possibility of creating images from inhomogeneous samples or to separate the signal of a sample container, *e.g.* a high-pressure cell, from the signal of the actual sample. In the latter case, this method is an efficient alternative to a collimating-slit design, which is often incompatible with the desire to collect the scattered intensity over a large solid angle as in the multiple-analyser spectrometer presented here. An example of an image of a H_2O sample, 350 μm in diameter, inside a Be gasket of a diamond-anvil cell, 5.5 mm in diameter, is shown in Fig. 6(*b*).

5. Contributions to the momentum and energy resolutions

In many applications of IXS a high resolution in both momentum and energy is important. The valence-electron excitations may be very sensitive to the momentum transfer magnitude $q = |\mathbf{q}|$, but core-electron excitations are much less so. The exact direction of $\mathbf{q}$ is important for anisotropic samples (*e.g.* single crystals). A multiple-element spectro-

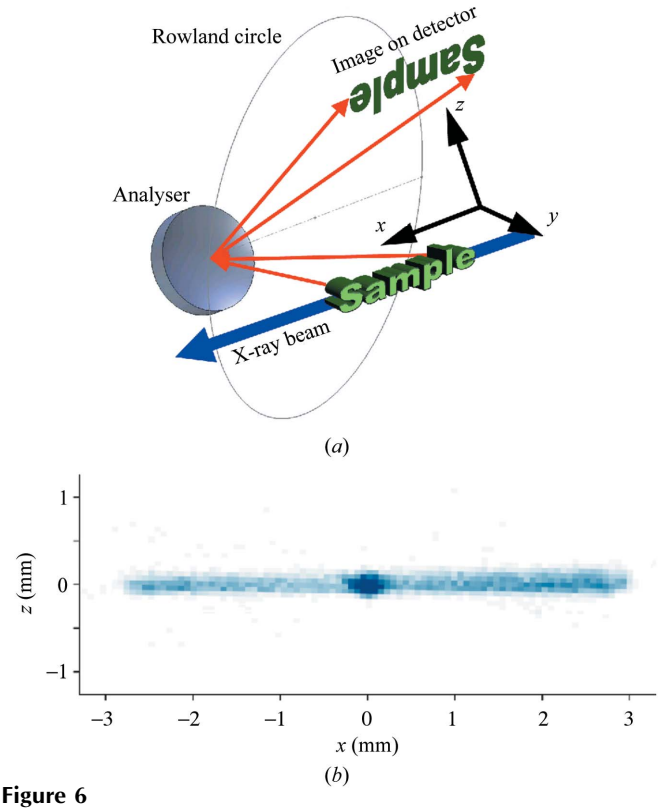

Figure 6
(*a*) Schematic idea of how point-to-point focusing of a spherically bent analyser crystal can be used for imaging a macroscopic sample which the X-ray beam penetrates through. (*b*) An image on a pixel detector at the peak of the quasi-elastic line showing an H_2O sample (at $x = z = 0$) inside a Be gasket. The contrast between the scattering cross sections of the sample and the gasket can be seen clearly, the sample giving higher intensity and appearing as an intense (here, dark) spot.

meter has the best efficiency for core excitations of directionally isotropic samples, as the information collected by all analysers can be used easily. In the case of single-crystal samples the scientific problem is typically to study the properties of the material along a certain, often high-symmetry, direction $\mathbf{q} \parallel \mathbf{G}$. If one analyser is aligned to collect the scattered intensity in that direction, the other analysers are not in high-symmetry directions but can still give useful information. Moreover, if the anisotropy is not very large, the **q**-resolution can be lowered by setting the nominal $\mathbf{q} \parallel \mathbf{G}$ in the middle of either a two-analyser column or in the middle of a four-analyser square to increase the collected solid angle. For applications requiring a high **q**-resolution, a reduction of the **q**-spread along an analyser crystal is also necessary and can be achieved by reducing the active area of the analyser crystal with horizontal slits.

The energy resolution is affected by various factors. These are a finite source size, aberration owing to the used Johann geometry, the off-Rowland contribution, and the intrinsic analyser crystal bandwidth. The incident-beam bandwidth naturally contributes directly to the final resolution, but we will restrict the discussion here to the contributions relevant to the spectrometer itself.

Analyser crystal bandwidth. The used Bragg angles $\theta_B = 87$–88° allow the reflectivity curves of the analysers to be calculated in the near-backscattering geometry. In the case of a diced analyser crystal, the intrinsic bandpass follows the Prince–Darwin curve, because each of the analyser cubes is a perfect single crystal and obeys the dynamic diffraction theory. The corresponding width of the reflectivity curve close to backscattering is 52 meV for Si(333) at 5.9 keV, 39 meV for Si(444) at 7.9 keV, 15 meV for Si(555) at 9.9 keV and 5 meV for Si(777) at 13.8 keV (Shvyd'ko, 2004). These are the typical energy ranges for the high-resolution experiments performed with the current instrument.

When a crystal is under stress, its X-ray reflectivity increases considerably (White, 1950). This is due to an increase of the reflectivity curve width, although the peak reflectivity is typically reduced. In fact, a monolithic bent crystal behaves within the kinematic diffraction limit. A reflectivity curve of such a crystal can be calculated from the theoretical formulation of Taupin and Takagi (Taupin, 1964; Takagi, 1962; Takagi, 1969). An approximative width of such a curve is

$$(\Delta E/E)_{\text{bending}} = (t/R)\left|\cot^2\theta_B - n_b\nu\right|, \qquad (3)$$

where t is the absorption length within the crystal and ν is the Poisson ratio of the crystal material. The parameter $n_b = 1$ for cylindrical or $n_b = 2$ for spherical bending.

Available bent analyser crystals used at ID16 are Si(*nnn*) ($n = 3, 4, 5$) and Si(*nn*0) ($n = 4, 6, 8$). Si(660) has a reflectivity larger by a factor of two compared with Si(555), so it is the reflection of choice if incident photon energies close to 10 keV are desired. The Si(660) and Si(555) crystals with 1 m bending radii have equal energy resolutions, dominated by the stress owing to the bending and not by the Darwin width. Si(444) can also be used owing to its slightly higher energy resolution at 7.9 keV, which is a result of the smaller penetration depth t of the lower-energy X-rays.

Fig. 7 shows the theoretically expected reflectivity curve of a bent Si(660) analyser crystal [convoluted with the incident-energy bandwidth of 200 meV obtained by using a Si(440) channel-cut at 9.69 keV] together with two experimentally

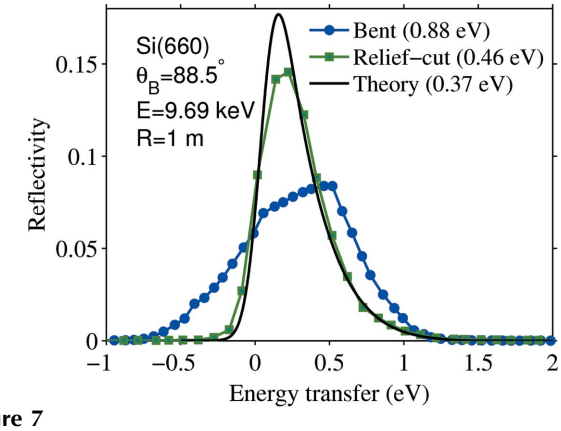

Figure 7
Theoretically expected reflectivity curve (broadened with the incident-photon beam bandwidth of the measurement conditions) together with experimentally observed resolution functions of two analyser crystals. The 'bent' crystal refers to the analyser (*b*) and the 'relief-cut' crystal to the analyser (*c*) of Fig. 4. The full width at half-maximum values of each curve are given in the legend.

measured ones, using a bent crystal (Fig. 4*b*) and one with stress-relief cuts (Fig. 4*c*) of 2.5 mm × 2.5 mm squares. The Bragg angle in the measurement was 88.5°. This shows that cutting the wafer to reduce the local stress is indeed an effective way to obtain reflectivity curves close to the theoretically expected ones.

Johann aberration. In the generally adopted Johann geometry the analyser crystal surface does not follow the Rowland circle. Thus the angle of incidence of the rays arriving at the crystal is smaller for the ray *i* arriving at the centre of the crystal (the nominal angle) than for a ray *j* that arrives at another part of the crystal. This introduces an aberration, which is roughly $(\Delta E/E)_{\rm Johann} = (1/2)\cot\theta_{\rm B}\varphi^2$, where φ is the angular difference in the dispersing direction between the rays *i* and *j*. It should be noted that the shape of the histogram corresponding to the Johann aberration along a crystal is far from being a Gaussian. The backscattering geometry of the analyser crystals renders the Johann aberration negligible in most cases, giving a broadening of only a few meV.

Contribution owing to deviations from the Rowland circle geometry. Generally, in a backscattering spectrometer it is not possible to place the detector exactly on the Rowland circle because the sample and its environment require a certain amount of space. Therefore, typically the detector is displaced from the Rowland circle. In the current spectrometer there are options to either align the detector on the Rowland circle (leaving about 40 mm of space above the sample) or move it towards the analysers at distances of d = 50–150 mm. If the analysers stay on the corresponding Rowland circles, they will no longer focus on the detector. For exact focusing conditions, the analysers can be translated away from the Rowland circle by a distance $z = d/2$. However, this causes the Bragg angles to vary along the analyser crystal surface, and the range of reflected energies is

$$(\Delta E/E)_{\rm Rowland} = \frac{zD}{(R\sin\theta_{\rm B} + z)^2}\cot\theta_{\rm B}, \qquad (4)$$

where D is the diameter of the active analyser crystal in the dispersing direction. This contribution can be reduced by choosing the analyser crystal position as close to the Rowland circle as possible, or by reducing the active analyser crystal area by slitting.

6. Examples of applications

The typical excitation of a valence electron gas in a solid-state system is the plasmon. In the random-phase approximation the plasmon is a well defined long-lived excitation, whose energy depends on the electron gas density only. The dynamic response from a simple plasmon-pole model can be modified by effects of band structure, correlation and low-lying core states which may partly overlap with valence electrons. This is exemplified by the valence spectra of V_2O_3 reported in Fig. 8, which show the valence-electron dynamics superimposed on V $3p_{1/2,3/2}$ (binding energy 37 eV) and V 3*s* (binding energy 66 eV) semicore-electron excitations. Similar spectra could be obtained with EELS for the lowest momentum transfers (Abe *et al.*, 1998). However, the non-trivial dispersion of these spectra could only be studied with IXS. At the largest momentum transfer the spectra are dominated by the above-mentioned core excitations. Full analysis of the spectra and details of the sample will be published elsewhere (Huotari, 2009).

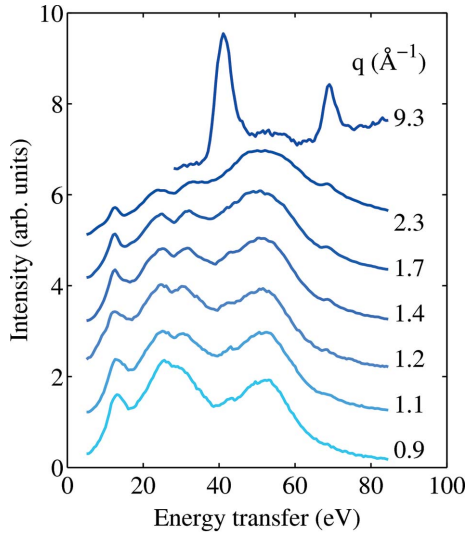

Figure 8
Valence-electron excitation spectra of V_2O_3 with $\mathbf{q} \parallel \mathbf{c}_{\rm h}$. The energy resolution was 1.5 eV with an analyser energy of 9.69 keV.

The study of core excitations using IXS instead of X-ray absorption spectroscopy (XAS) is a quickly developing field. This method is especially useful in studies of low-energy absorption edges up to about 1 keV, where the corresponding XAS experiments fall in the soft X-ray regime. Recent reviews of these studies can be found by Bergmann *et al.* (2002), Schülke (2007) and Sternemann *et al.* (2008*a*). The experiments are not surface sensitive, and do not require a vacuum environment. This makes it possible to perform the experiments even for embedded samples (below a surface, inside a high-pressure gasket or other cells) and samples not compatible with vacuum. In particular, the potential for high-pressure applications is enormous (Mao *et al.*, 2001, 2003; Lee *et al.*, 2005; Meng *et al.*, 2004). Up to now, XANES regions of *K* edges up to fluorine (Hämäläinen *et al.*, 2002) have been accessed, as well as *L* edges up to silicon (Sternemann *et al.*, 2007), and even $N_{4,5}$ edges of Ba (Sternemann *et al.*, 2008*a*), Ce and La (Gordon *et al.*, 2008). Also EXAFS regions of the *K* edges of light elements (Bergmann *et al.*, 2007) can be studied. Moreover, the excitation channels are not limited to the dipole-allowed ones, and by varying the momentum-transfer magnitude monopole and quadrupole transitions can be studied, giving the possibility of measuring the angular-momentum-projected density of states for different symmetries (Doniach *et al.*, 1971; Krisch *et al.*, 1997; Soininen *et al.*, 2005, 2006), thus yielding information not accessible by other techniques.

As an example, the dynamic structure factor of diamond powder is reported in Fig. 9 for various momentum transfers.

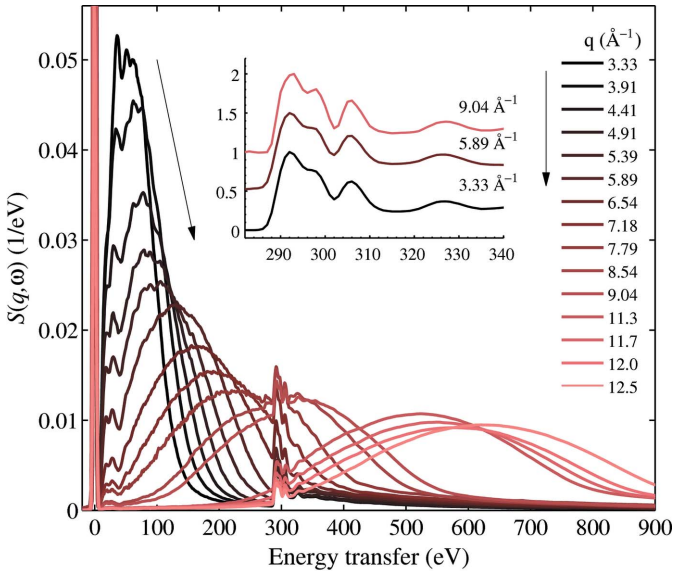

Figure 9
Measured $S(q, \omega)$ of diamond for selected momentum-transfer values. The broad valence contribution moves to higher energies with increasing q as shown by the arrow. The inset shows near-edge spectra which are corrected for the pre-edge background and normalized to unity edge jump.

These measurements have been performed using a combination of different analyser reflections and scattering angles 2θ to span the range q = 2.6–12.6 Å^{-1}. In particular, bent Si(nn0) analyser crystals were used with reflection orders n = 6 and 8. The measurements were performed on a 2 mm-thick pressed pellet of diamond powder (grain size <1 µm) in vacuum at room temperature. The energy resolution was 1.6–2.0 eV, optimized for maximum flux. Near-edge spectra are shown in the inset. The valence electron contribution can be seen dispersing strongly as a function of momentum transfer q, transforming from a plasmon-like peak at low q to the Compton profile at high q. The plasmon peak has additional low-energy features owing to band-structure effects. The carbon K-edge near 285 eV marks the onset of scattering from 1s electrons, and exhibits the usual XANES structure followed by the EXAFS region. The extraction of the XANES structures from the valence-electron background has to be done carefully (Sternemann *et al.*, 2008*b*), especially so if the EXAFS region is to be studied (Pylkkänen *et al.*, 2009).

With the present spectrometer, it is also possible to perform IXS experiments with energy resolution better than 100 meV using diced analyser crystals (Huotari *et al.*, 2005, 2006). Typical energy resolution is 50 meV at 7.91 keV (Si 444 reflection), 30 meV at 9.89 keV (Si 555) and 10 meV at 13.8 keV (Si 777). The relevant excitation-energy range that it is possible to study using this method is typically 1–10 eV, well suited for studies of well localized valence-electron excitations, low-energy plasmons *etc.* As an example, the crystal-field excitations in NiO powder are shown in Fig. 10. Six diced Si(444) analyser crystals were used with the spectrometer covering scattering-angle ranges of 131–150°, corresponding to a range of momentum transfers of 7.3–8.0 Å^{-1}. These spectra display excitations within the 3d band of the Ni^{2+} ion

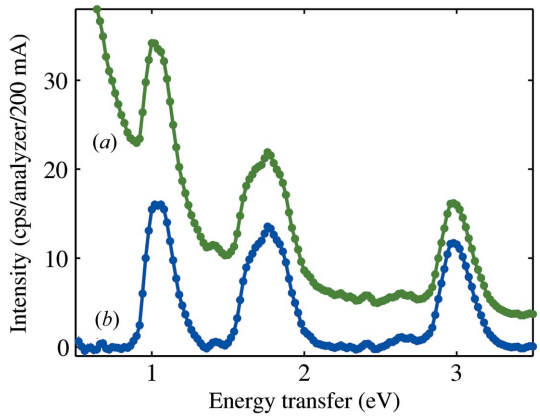

Figure 10
Crystal-field excitations in NiO powder (T = 7 K) averaged over q = 7.3–8.0 Å^{-1}, both before (a) and after (b) the subtraction of the sloping quasi-elastic line background. The energy resolution was 50 meV and the analyser energy was 7.91 keV.

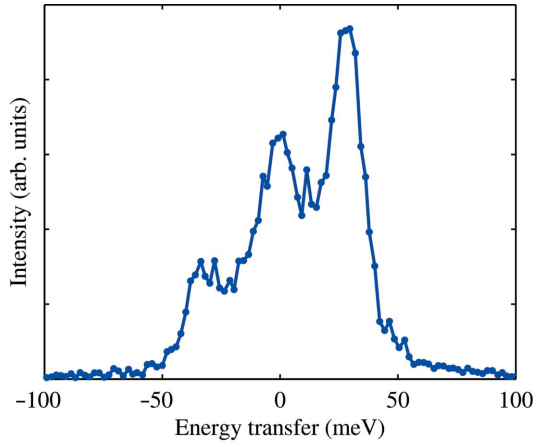

Figure 11
Acoustic phonons in aluminium at room temperature, measured with a resolution of 10 meV with an analyser energy of 13.8 keV. Here the momentum transfer was $\mathbf{q}$ = 1.8 Å^{-1} along the [110] direction.

(Larson *et al.*, 2007). These excitations have also been studied and characterized in detail by using EELS (Fromme, 2001) and RIXS at the Ni K, L or M edges (Huotari *et al.*, 2008; Chiuzbăian *et al.*, 2005). It is noteworthy that the tail of the quasi-elastic line always gives a background at these low energy transfers so that it has to be subtracted. It is even possible to obtain phonon spectra in selected materials with high efficiency, as in the case of the acoustic phonons in aluminium shown in Fig. 11. In this example, the spectrometer used the Si(777) reflection of a diced analyser crystal fixed at a momentum transfer $|\mathbf{q}|$ = 1.8 Å^{-1} with $\mathbf{q} \parallel$ [110]. This spectrum reflects the highest energy resolution obtainable at the moment with the 1 m spectrometer described here.

7. Conclusions

A spectrometer for NRIXS based on nine analyser crystals and a position-sensitive detector has been developed at the European Synchrotron Radiation Facility beamline ID16. Applications concentrate on non-resonant inelastic X-ray

scattering experiments to study electronic excitations with energy resolutions of 10–2000 meV. The energy-transfer range is practically unlimited, and examples of applications are shown for energy transfers up to 1000 eV. The typical accessible momentum-transfer range is 0.3–13 Å^{-1}. The incident-photon energies are usually in the 6–13 keV range. Both valence and core-electron excitations can be studied even in relatively high-Z samples. Examples of applications include both collective and single-particle valence-electron excitations, core electrons excitations and even phonons.

The authors would like to thank Valentina Giordano, Pieter Glatzel, Keijo Hämäläinen, Laurent Jacqmin, Michael Krisch, Marie-Claire Lagier, Luigi Paolasini, Emmanuel Papillon, Cyril Ponchut, Juha Aleksi Soininen and Christian Sternemann. GV acknowledges the support from the Bolyai János Fellowship.

References

Abe, H., Terauchi, M., Tanaka, M. & Shin, S. (1998). *Jpn. J. Appl. Phys.* **37**, 584–588.

Alessandrello, A., Beeman, J. W., Brofferio, C., Cremonesi, O., Fiorini, E., Giuliani, A., Haller, E. E., Monfardini, A., Nucciotti, A., Pavan, M., Pessina, G., Previtali, E. & Zanotti, L. (1999). *Phys. Rev. Lett.* **82**, 513–515.

Bergmann, U., di Cicco, A., Wernet, P., Principi, E., Glatzel, P. & Nilsson, A. (2007). *J. Chem. Phys.* **127**, 174504.

Bergmann, U. & Cramer, S. P. (1998). *Proc. SPIE*, **3448**, 198–209.

Bergmann, U., Glatzel, P. & Cramer, S. P. (2002). *Microchem. J.* **71**, 221–230.

Cai, Y. Q., Chow, P., Chen, C. C., Ishii, H., Tsang, K. L., Kao, C. C., Liang, K. S. & Chen, C. T. (2004). *AIP Conf. Proc.* **705**, 340–343.

Chiuzbăian, S. G., Ghiringhelli, G., Dallera, C., Grioni, M., Amann, P., Wang, X., Braicovich, L. & Patthey, L. (2005). *Phys. Rev. Lett.* **95**, 197402.

Doniach, S., Platzman, P. M. & Yue, J. T. (1971). *Phys. Rev. B*, **4**, 3345–3350.

Fister, T. T., Seidler, G. T., Wharton, L., Battle, A. R., Ellis, T. B., Cross, J. O., Macrander, A. T., Elam, W. T., Tyson, T. A. & Qian, Q. (2006). *Rev. Sci. Instrum.* **77**, 063901.

Frank, M., Mears, C. A., Labov, S. E., Azgui, F., Lindeman, M. A., Hiller, L. J., Netel, H. & Barfknecht, A. (1996). *Nucl. Instrum. Methods Phys. Res. A*, **370**, 41–43.

Fromme, B. (2001). *d–d Excitations in Transition Metal Oxides.* Berlin: Springer-Verlag.

Galambosi, S., Knaapila, M., Soininen, J. A., Nygård, K., Huotari, S., Galbrecht, F., Scherf, U., Monkman, A. P. & Hämäläinen, K. (2006). *Macromolecules*, **39**, 9261–9266.

García de Abajo, F. J. (2009). *Rev. Mod. Phys.* In the press; arxiv:0903.1669v1 [cond-mat.mtrl-sci].

Gordon, R. A., Seidler, G. T., Fister, T. T., Haverkort, M. W., Sawatzky, G. A., Tanaka, A. & Sham, T. K. (2008). *Europhys. Lett.* **81**, 26004.

Hämäläinen, K., Galambosi, S., Soininen, J. A., Shirley, E. L., Rueff, J.-P. & Shukla, A. (2002). *Phys. Rev. B*, **65**, 155111.

Hazemann, J.-L. *et al.* (2009). *J. Synchrotron Rad.* **16**, 283–292.

Hill, J. P., Coburn, D. S., Kim, Y.-J., Gog, T., Casa, D. M., Kodituwakku, C. N. & Sinn, H. (2007). *J. Synchrotron Rad.* **14**, 361–365.

Huotari, S., (2009). In preparation.

Huotari, S., Albergamo, F., Vankó, G., Verbeni, R. & Monaco, G. (2006). *Rev. Sci. Instrum.* **77**, 053102.

Huotari, S., Pylkkänen, T., Vankó, G., Verbeni, R., Glatzel, P. & Monaco, G. (2008). *Phys. Rev. B*, **78**, 041102(R).

Huotari, S., Vankó, Gy., Albergamo, F., Ponchut, C., Graafsma, H., Henriquet, C., Verbeni, R. & Monaco, G. (2005). *J. Synchrotron Rad.* **12**, 467–472.

Krisch, M. H., Sette, F., Masciovecchio, C. & Verbeni, R. (1997). *Phys. Rev. Lett.* **78**, 2843–2846.

Larson, B. C., Ku, W., Tischler, J. Z., Lee, C.-C., Restrepo, O. D., Eguiluz, A. G., Zschack, P. & Finkelstein, K. D. (2007). *Phys. Rev. Lett.* **99**, 026401.

Lee, S. K., Eng, P. J., Mao, H.-K., Meng, Y., Newville, M., Hu, M. Y. & Shu, J. (2005). *Nat. Mater.* **4**, 851–854.

Llopart, X., Campbell, M., Dinapoli, R., San Segundo, D. & Pernigotti, E. (2002). *IEEE Trans. Nucl. Sci.* **49**, 2279–2283.

Mao, H.-K., Kao, C.-C. & Hemley, R. J. (2001). *J. Phys.: Condens. Matter*, **13**, 7847–7858.

Mao, W. L., Mao, H.-K., Eng, P. J., Trainor, T. P., Newville, M., Kao, C.-C., Heinz, D. L., Shu, J., Meng, Y. & Hemley, R. J. (2003). *Science*, **302**, 425–427.

Masciovecchio, C., Bergmann, U., Krisch, M., Ruocco, G., Sette, F. & Verbeni, R. (1996). *Nucl. Instrum. Methods Phys. Res. B*, **111**, 181–186.

Mears, C. A., Labov, S. E., Frank, M., Lindeman, M. A., Hiller, L. J., Netel, H. & Barfknecht, A. T. (1996). *Nucl. Instrum. Methods Phys. Res. A*, **370**, 53–56.

Meng, Y., Mao, H.-K., Eng, P. J., Trainor, T. P., Newville, M., Hu, M. Y., Kao, C.-C., Shu, J., Hausermann, D. & Hemley, R. J. (2004). *Nat. Mater.* **3**, 111–114.

Owen, R. L., Holton, J. M., Schulze-Briese, C. & Garman, E. F. (2009). *J. Synchrotron Rad.* **16**, 143–151.

Pylkkänen, T., Soininen, J. A., Monaco, G. & Huotari, S. (2009). In preparation.

Schülke, W. (2007). *Electron Dynamics by Inelastic X-ray Scattering.* Oxford University Press.

Schwoerer-Böhning, M., Macrander, A. T., Abbamonte, P. M. & Arms, D. A. (1998). *Rev. Sci. Instrum.* **69**, 3109–3112.

Shew, B.-Y., Huang, R.-S., Wang, D.-J., Perng, S.-Y., Kuan, C.-K., Cai, Y. Q., Chow, P., Schwoerer-Böhning, M., Caliebe, W., Kao, C.-C. & Chen, C. T. (2002). *Proc. SPIE*, **4783**, 131–138.

Shvyd'ko, Y. V. (2004). *X-ray Optics.* Berlin: Springer-Verlag.

Soininen, J. A., Ankudinov, A. L. & Rehr, J. J. (2005). *Phys. Rev. B*, **72**, 045136.

Soininen, J. A., Mattila, A., Rehr, J. J., Galambosi, S. & Hämäläinen, K. (2006). *J. Phys.: Condens. Matter*, **18**, 7327–7336.

Sternemann, C., Sternemann, H., Huotari, S., Lehmkühler, F., Tolan, M. & Tse, J. S. (2008*a*). *J. Anal. At. Spectrom.* **23**, 807–813.

Sternemann, H., Soininen, J. A., Sternemann, C., Hämäläinen, K. & Tolan, M. (2007). *Phys. Rev. B*, **75**, 075118.

Sternemann, H., Sternemann, C., Seidler, G. T., Fister, T. T., Sakko, A. & Tolan, M. (2008*b*). *J. Synchrotron Rad.* **15**, 162–169.

Takagi, S. (1962). *Acta Cryst.* **15**, 1311–1312.

Takagi, S. (1969). *J. Phys. Soc. Jpn*, **26**, 1239–1253.

Taupin, D. (1964). *Bull. Soc. Fr. Mineral. Crystallogr.* **87**, 469–511.

Verbeni, R., Kocsis, M., Huotari, S., Krisch, M., Monaco, G., Sette, F. & Vankó, G. (2005). *J. Phys. Chem. Solids*, **66**, 2299–2305.

White, J. E. (1950). *J. Appl. Phys.* **21**, 855–859.